ELSEVIER

Volume 183, Issue 5, May 2010

JOURNAL OF SOLID STATE CHEMISTRY

www.elsevier.com/locate/jssc

CONTENTS

Abstracted/indexed in BioEngineering Abstracts, Chemical Abstracts, Coal Abstracts, Current Contents/Physics, Chemical, & Earth Sciences, Engineering Index, Research Alert, SCISEARCH, Science Abstracts, and Science Citation Index. Also covered in the abstract and citation database SCOPUS®. Full text available on ScienceDirect®.

Regular Articles

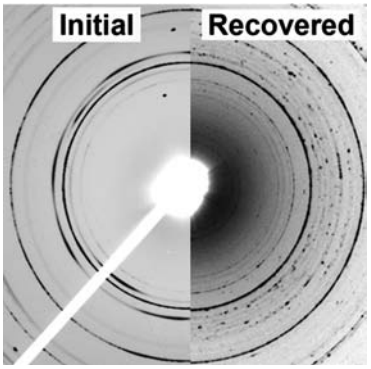

Selected images recorded with a MAR345 image plate detector show the reaction of α-Sc and graphite at high-(P,T) conditions. Left: mixture of α-Sc and graphite. Right: recovered sample after laser heated the diamond anvil cell.

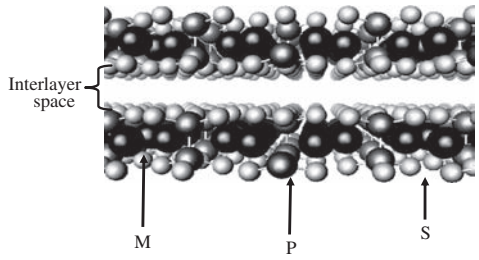

Atomic building of MPS_3.

Regular Articles—Continued

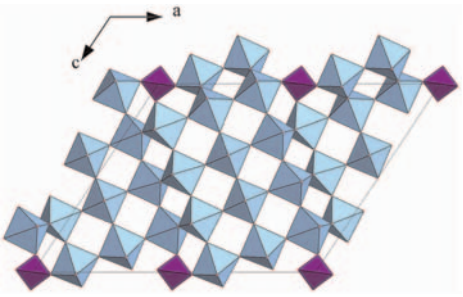

The projected structure can be described as $3 \times 4 \times \infty$ ReO_3 type blocks of NbO_6 octahedra sharing corners, joined with identical blocks via tetrahedrally coordinated tungsten atoms.

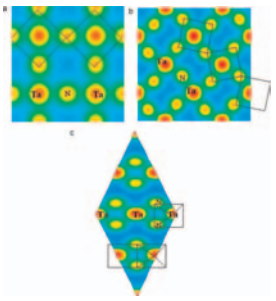

$ThTaN_3$: Projected charge density (for 4 fu) onto basal plane: (a) cubic perovskite, (b) orthorhombic perovskite and (c) post-perovskite. Red, green and blue areas are relevant to strong, medium and low localization of density.

Continued

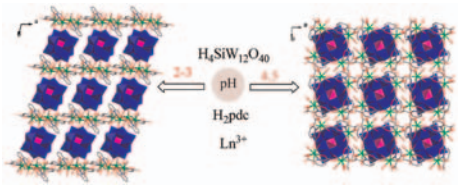

Two types of new inorganic–organic hybrid frameworks through incorporation of Keggin-type heteropolyanion $[SiW_{12}O_{40}]^{4-}$ within the voids of lanthanides-pdc network as pillars or guests under hydrothermal condition were successfully assembled. Solid-state properties of compounds **1** and **2a** such as thermal stability and photoluminescence have been further investigated.

A series of $Sr_2MMoO_{6-\delta}$ compounds with M = Mg, Mn, Fe, Co, Ni and Zn is investigated for their crystal structure, redox stability and precise oxygen content in order to address systematically the questions concerning the cation (dis)order, oxygen (non)stoichiometry and valence mixing in *B*-site ordered double-perovskite oxides.

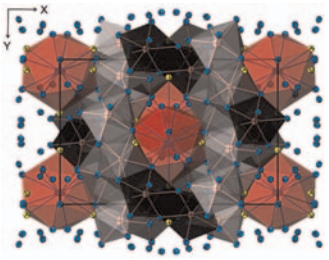

Crystal structure of $CePd_8B_{2-x}$.

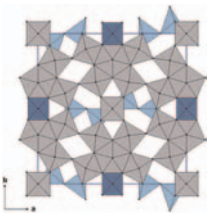

A crystal structural model for the orthorhombic compound $V_{2.38}Nb_{10.7}O_{32.7}$, which is known as "$V_2Nb_9O_{27.5}$", was developed by means of selected area electron diffraction, Rietveld refinement and high resolution electron microscopy. In dependence on the synthesis method the metastable compound is obtained as chain-like agglomerated nanoparticles or as more compact micro-scaled crystals. $V_{2.38}Nb_{10.7}O_{32.7}$ is the first and only example of a compound with a TTB-type structure (space group *Cmmm*) in the system V_2O_5–Nb_2O_5.

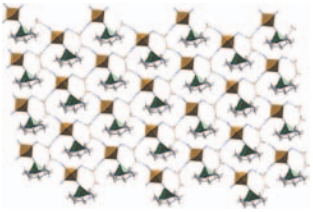

Three heterobimetallic cyano-bridged copper(II) nitroprusside-based complexes of the general compositions of $[Cu(L)Fe(CN)_5NO] \cdot xH_2O$, where L = *N,N'*-bis(3-aminopropyl)ethylenediamine (complex **1**), 1,3,6,9,11,14-hexaazatricyclo[12.2.1.1^{6,9}]-octadecane (complex **2**) and *N*-methylethylenediamine (complex **3**), were synthesized, and fully structurally and magnetically characterized. SEM, EDS, XRD and ^{57}Fe Mössbauer experiments were used for characterization of thermal decomposition products of complexes **2** and **3**.

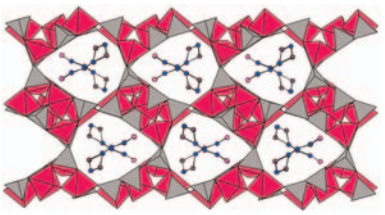

The aluminophosphate analogue of open-framework gallophosphate ULM-3 was synthesized in the presence of 3-methylaminopropylamine. The *Pcab* crystal symmetry and hydrogen bonding scheme was determined by single-crystal X-ray diffraction and NMR spectroscopy.

Estimation of the intrinsic stresses in α-alumina in relation with its elaboration mode
A. Boumaza and A. Djelloul
Page 1063

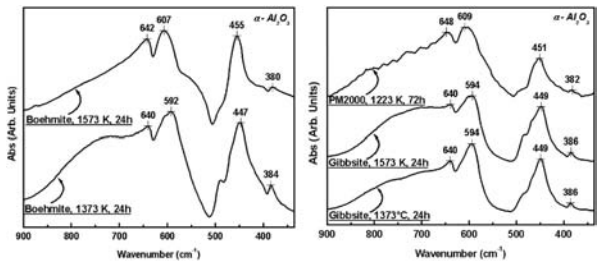

The infrared peak at 378.7 cm^{-1} was used as a reference for stress free α-alumina and the shift of this peak allowed to estimate intrinsic stresses, which were related to the morphology and to the specific surface area of aluminas according to their elaboration mode.

Non-random cation distribution in hexagonal $Al_{0.5}Ga_{0.5}PO_4$
S.K. Kulshreshtha, O.D. Jayakumar and V. Sudarsan
Page 1071

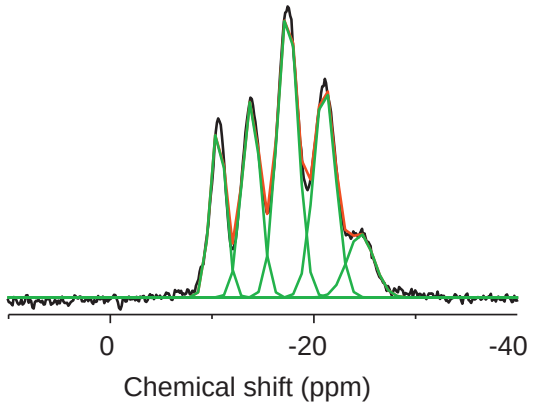

^{31}P MAS NMR pattern of hexagonal $Al_{0.5}Ga_{0.5}PO_4$ solid solution.

Hydrogen production from water decomposition by redox of Fe_2O_3 modified with single- or double-metal additives
Xiaojie Liu and Hui Wang
Page 1075

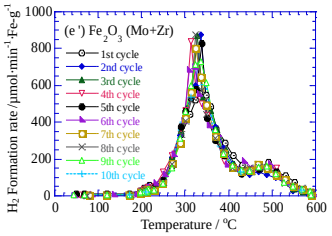

Mo + Zr additive has the best modified effect on improving the redox performances of Fe_2O_3:H_2 producing temperature of 276 °C and hydrogen storage capacity of 4.73 wt%.

Effects of the *A*-site cation number on the properties of $Ln_{5/8}M_{3/8}MnO_3$ manganites
J.A. Collado, J.L. García-Muñoz and M.A.G. Aranda
Page 1083

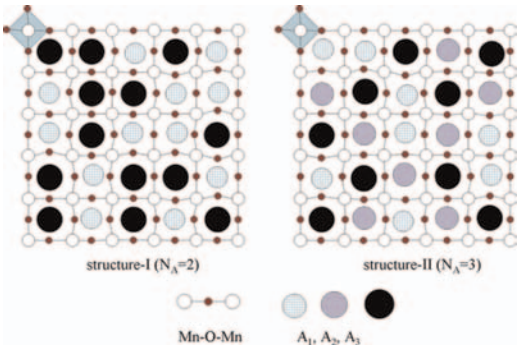

In this paper the influence of *A*-site cation number is shown, see attached schematic figure, on the magnetotransport properties of T_c-optimized manganites, $Ln_{5/8}M_{3/8}MnO_3$.

Chemical route for formation of intermetallic Zn_4Sb_3 phase
A. Denoix, A. Solaiappan, R.M. Ayral, F. Rouessac and J.C. Tedenac
Page 1090

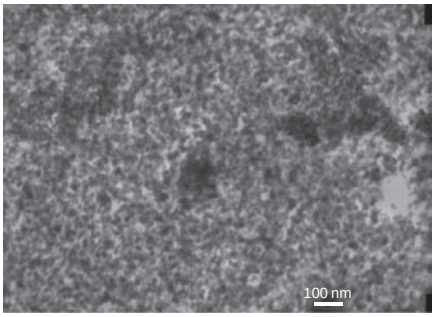

TEM observation of the Zn_4Sb_3 powder synthesized by soft chemistry.

Structural and conductivity studies of $Y_{10-x}La_xW_2O_{21}$
Anna Lashtabeg, John Bradley, Andrew Dicks, Graeme Auchterlonie and John Drennan
Page 1095

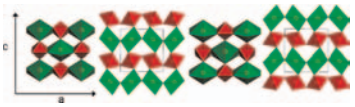

The solubility limit of La_2O_3 in $Y_{10}W_2O_{21}$ was found to be > 50% after which the structure was found to change to Weberite type structure, A′ A″B′ B″O_7 that is closely related to the pyrochlore.

Continued

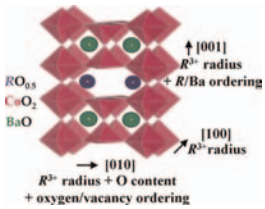

The entire family of carefully oxygen-adjusted RBaCo$_2$O$_{5.5}$ (R = Y, La–Ho) double-perovskite cobalt oxides is systematically studied for lattice parameters and peculiar physical properties. The results indicate R/Ba cation and oxygen/vacancy disorders for the largest R constituents with Nd, Pr and La. The physical properties are found to be sensitive even for tiny deviations from the ideal 5.5 oxygen stoichiometry.

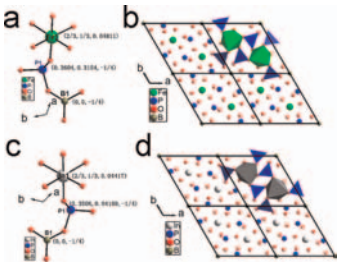

Two anhydrous metal borophosphates of $M_2^{III}BP_3O_{12}$ (M = Fe, In) have been prepared and characterized. They both crystallize in the hexagonal system, space group $P6(3)/m$ (no. 176) and feature 3D architectures build up of the M_2O_9 units and $B(PO_4)_3$ groups via sharing the corners, but they are not isomorphic for the different crystallographically distinct atomic positions.

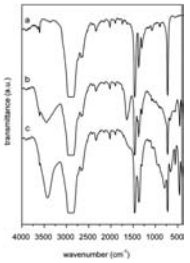

Intercalation of iminodiacetic acid (IDA) anions in a MgAl-NO_3-layered double hydroxide host leads to an enhancement of its infrared absorbing ability for application in agricultural plastic films.

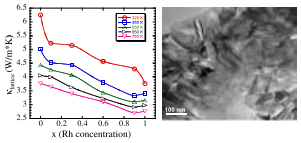

Significant reduction of the lattice thermal conductivity with increasing Rh concentration in the p-type $Zr_{0.5}Hf_{0.5}Co_{1-x}Rh_xSb_{0.99}Sn_{0.01}$ half-Heusler materials prepared by solid state reaction at 1173 K.

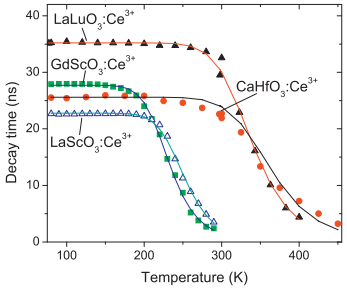

Ce^{3+} decay times versus temperature for perovskites with nd^0 B-site cations, specifically Ca(Hf,Zr)O_3 and (La,Gd)ScO_3, is investigated in this report.

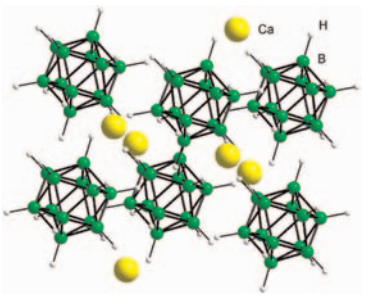

Calcium dodecahydro-*closo*-dodecaborate, $CaB_{12}H_{12}$ (**1**), was isolated by dehydration/desolvation of $[Ca(H_2O)_7][B_{12}H_{12}]\cdot H_2O$ (**2**) or $[Ca(H_2O)_5(MeCN)_2][B_{12}H_{12}]$ (**3**). The crystal structure of **1** was determined by powder X-ray diffraction and confirmed by neutron vibrational spectroscopy and first-principles calculations. Hydrogen storage properties of **1** in the presence of calcium hydride were elucidated.

Application of Brazilian kaolinite clay as adsorbent to removal of U(VI) from aqueous solution: Kinetic and thermodynamic of cation–basic interactions
Denis L. Guerra, Victor L. Leidens, Rúbia R. Viana and Claudio Airoldi
Page 1141

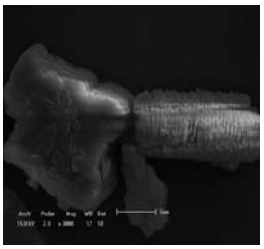

This investigation reports the use of original and modified kaolinites as alternative absorbents. The compound N-[3-trimethoxysilyl)propyl]diethylenetriamine was anchored onto Amazon kaolinite surface by heterogeneous route.

Two anionic $[Cu^{I}_{6}X_7]_n^{n-}$ (X = Br and I) chain-based organic–inorganic hybrid solids with *N*-substituted benzotriazole ligands
Xia Gao, Quan-Guo Zhai, Shu-Ni Li, Rui Xia, Hai-Juan Xiang, Yu-Cheng Jiang and Man-Cheng Hu
Page 1150

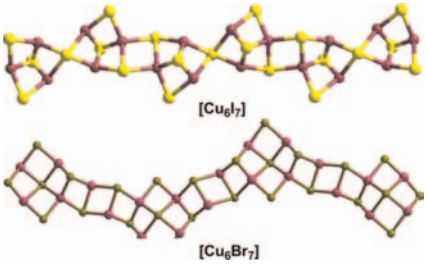

Two unprecedented anionic $[Cu^{I}_{6}X_7]_n^{n-}$ (X = Br and I) chain-based organic–inorganic hybrid solids, namely, $\{(HETA)[(Cu_6I_7)(ETA)_2]\}_n$ (1) and $\{K(Cu_6Br_7)(BBTH)\}_n$(2) (ETA = *N*-ethylbenzotriazole, HETA = protonated *N*-ethylbenzotriazole, BBTH = 1,6-bi(benzotriazole)- hexane) have been synthesized under solvothermal reactions and characterized.

Lanthanide oxalatophosphonates with two- and three-dimensional structures
Ting-Hai Yang, Deng-Ke Cao, Yi-Zhi Li and Li-Min Zheng
Page 1159

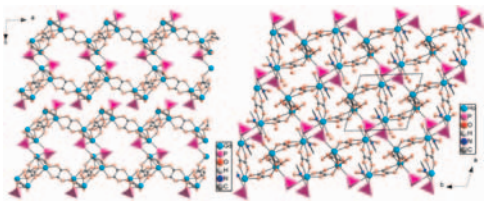

Compounds $[Ln_4(ox)_5(2\text{-pmpH})_2(H_2O)_7]\cdot 5H_2O$ (Ln = Gd, Tb, Dy; 2-pmp = 2-pyridylmethylphosphonate) and $[Ln_4(ox)_5(2\text{-pmpH})_2(H_2O)_6]\cdot 6H_2O$ (Ln = Ho, Yb) with 2D and 3D structures, respectively, are reported.

Structural variations of Sn^{II} pyridylphosphonates influenced by an uncommon Sn–N interaction
Houston Perry, Jerzy Zoń, Justin Law and Abraham Clearfield
Page 1165

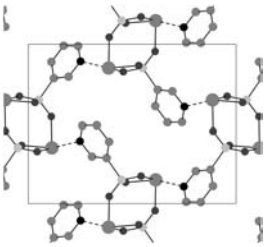

Interactions between pyridyl nitrogen atoms and Sn^{II} affect the packing of tin phosphonate ladders in the structures of Sn^{II} pyridylphosphonates.

Prediction and assignment of site occupation and energy levels for Pb^{2+} ions in crystal hosts
Qiang Sun, Jing Wang and Jinsheng Shi
Page 1174

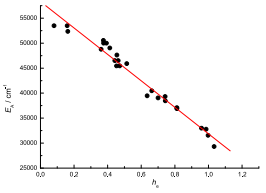

The A band energy E_A of Pb^{2+} has linear relationship with environmental factor h_e.

Crystal structure and electronic properties of the new compounds $U_3Co_{12-x}X_4$ with X = Si, Ge
A. Soudé, O. Tougait, M. Pasturel, D. Kaczorowski and H. Noël
Page 1180

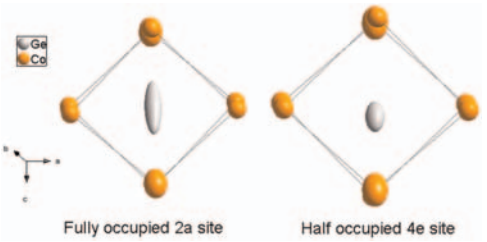

The crystal structure of the new compounds $U_3Co_{12-x}X_4$, X = Si, Ge is a ternary ordered variant of the $EuMg_{5.2}$-type with a site preference for the *4e* position.

Continued

Synthesis and crystal structure of $Ln_2M^{2+}Ge_4O_{12}$, Ln = rare-earth element or Y; M = Ca, Mn, Zn
Vladimir G. Zubkov, Nadezda V. Tarakina, Ivan I. Leonidov, Alexander P. Tyutyunnik, Ludmila L. Surat, Marina A. Melkozerova, Elena V. Zabolotskaya and Dina G. Kellerman
Page 1186

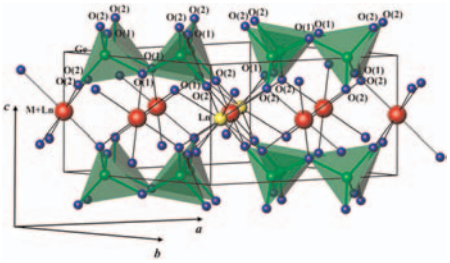

Crystal structure of $Ln_2MGe_4O_{12}$, where Ln = rare-earth element or Y; M = Ca, Mn, Zn.

Investigation on the structural and electrical properties of $NdSrNi_{1-x}Cr_xO_{4+\delta}$ ($0.1 \le x \le 0.9$) system
Manel Jammali, H. Chaker, K. Cherif and R. Ben Hassen
Page 1194

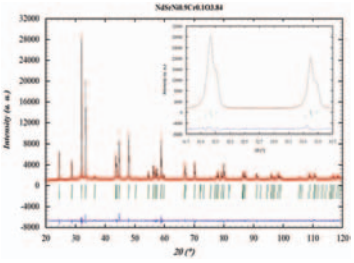

The X-ray pattern of the $x = 0.1$ sample showed a shift of some Bragg reflections that was indicative of a unit cell of lower symmetry. Two distortions of the $I4/mmm$ K_2NiF_4 aristotype cell to orthorhombic symmetry are known, $Fmmm$ and $I\,mmm$, depending on which of the $\langle 100 \rangle$ and $\langle 110 \rangle$ sets of mirror planes and twofold axes are lost together with the fourfold axis when the symmetry is lowered.

Rapid Communications

Synthesis and crystal structure of new layered $BaNaSc(BO_3)_2$ and $BaNaY(BO_3)_2$ orthoborates
Yurii V. Seryotkin, Vladimir V. Bakakin, Aleksandr E. Kokh, Nadezhda G. Kononova, Tatyana N. Svetlyakova, Konstantin A. Kokh and Tatyana N. Drebushchak
Page 1200

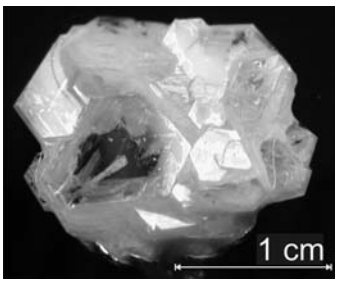

The distinctive feature of new orthoborate crystals $BaNaSc(BO_3)_2$ and $BaNaY(BO_3)_2$ is the combination of base building packages of two types: $\{M^{3+}[Ba^{2+}(BO_3)^{3-}]_2\}^{+}$ and $\{M^{3+}[Na^{+}(BO_3)^{3-}]_2\}^{-}$, where M is Sc or Y.

Phase transitions, electrical conductivity and chemical stability of $BiFeO_3$ at high temperatures
Sverre M. Selbach, Thomas Tybell, Mari-Ann Einarsrud and Tor Grande
Page 1205

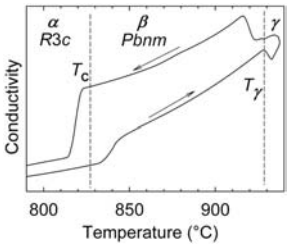

The structural phase transitions of multiferroic $BiFeO_3$ are shown to first order, with discontinuous volume and electrical conductivity. Semiconductivity was found for all three polymorphs of $BiFeO_3$.